Destructive potential of planetary meteotsunami waves beyond the Hunga volcano eruption (Tonga)

Cléa Denamiel[1,*], Sergiy Vasylkevych[2], Nedjeljka Žagar[2], Petra Zemunik[3], Ivica Vilibić[1]

[1]Ruđer Bošković Institute, Division for Marine and Environmental Research, Bijenička cesta 54, 10000 Zagreb, Croatia

[2]Universität Hamburg, Meteorological Institute, Grindelberg 5, 20144 Hamburg, Germany

[3]Institute of Oceanography and Fisheries, Šetalište I. Meštrovića 63, 21000 Split, Croatia

*Corresponding author. cdenami@irb.hr, ORCiD: 0000-0002-5099-1143

Abstract:

Worldwide tsunamis generated by atmospheric waves – or planetary meteotsunami waves – are extremely rare events occurring during supervolcano explosions or asteroid impacts. Recently, such waves have been globally recorded after the Hunga volcano eruption (Tonga) but did not pose any serious danger to the coastal communities. However, this study highlights that the mostly ignored destructive potential of planetary meteotsunami waves can be compared to the well-studied tsunami hazards. Through simple numerical experiments we indeed prove that meteotsunami surges above 1.00 m can be generated along more than 7 % of the world coastlines by atmospheric waves either more intense or slower than during the Hunga event. Consequently, the global meteotsunami hazards should now be properly assessed to prepare for the next big volcanic eruption or asteroid impact.

One-Sentence Summary:

During volcanic eruptions or asteroid impacts, global meteotsunami surges can be as destructive as localized tsunamis.

Catastrophic events such as volcano explosions (*1*) or asteroid impacts (*2, 3*) are known to cause extreme damages near their epicentres but also to affect the entire planet through megatsunamis (*4*), acidification of the atmosphere and ocean (*5*), aerosol-driven reduction of solar radiation (*6*), and many other planetary-scale processes. However, the global impact of atmospheric waves (*7*) generated during these events, including acoustic-gravity waves (*8*) and the most prominent Lamb waves (*9, 10*), remains sporadically documented. Lamb waves propagate horizontally in the atmosphere with a speed close to the mean sound speed (*11*) and can circle the globe multiple times (*12, 13*). They are associated with surface pressure oscillations of several hectopascals (hPa) per minute (*12, 14*) and their energy is dissipated towards the thermosphere (*15*) via the ionosphere. In the worldwide oceans, they excite atmospheric tsunamis or meteotsunamis – long-waves in the tsunami frequency band generated by atmospheric disturbances (*16, 17*) – which spread with much greater speeds than tsunami waves generated by volcanic eruptions or seismic activity (*18, 19*).

The existence of planetary-scale Lamb wave-driven meteotsunamis has been first hypothesized after the catastrophic eruption of the Krakatau volcano in 1883 (*12, 20*). The then sparse and low-quality tide-gauge global network recorded (a) a mismatch between the analytically derived and observed arrival times of the tsunami waves resulting from the volcano collapse in the Pacific Ocean, and (b) worldwide sea level oscillations as far away from the source as the English Channel. Nowadays, meteotsunamis locally generated by weather systems are known to be fully amplified when an atmospheric disturbance travels at a speed U similar to the ocean waves ($c=\sqrt{gH}$, with g the gravity and H the ocean depth) – i.e., when the Froude number ($Fr=U/c$) is close to 1.0 (*21*). Under this condition, also referred as Proudman resonance (*22*), the energy of the atmospheric disturbance is fully transferred to the background ocean waves which are amplified by an order of magnitude compared to the inverse barometer effect (*21*). In terms of coastal risks, the meteotsunami surges (i.e., the maximum coastal sea levels) can be of the order of several meters as observed in the Adriatic Sea in 1978 (*16, 17*). They can thus cause extensive infrastructure damage, navigation and beach safety concerns and human casualties (*16, 17*). However, the socio-economic impact of meteotsunamis generated by weather systems is generally geographically limited to bays and littoral areas (at most a hundred of kilometres of coastline).

The recent explosive eruption of the Hunga Tonga–Hunga Ha'apai volcano (Hunga eruption hereafter) on 15 January 2022 (*7, 13, 14, 19, 23*) was exceptionally well observed by satellites and recorded worldwide by thousands of microbarographs, seismometers and tide-gauges (*7, 14, 23*). This rare event thus provided a unique opportunity for the scientific community to revisit the global impact of meteotsunamis. Consequently, in this study, we assess the destructive potential of the planetary meteotsunami waves, beyond the Hunga eruption, with state-of-the-art atmospheric and oceanic global models. First, we simulate the main wave signals of the Hunga event to describe the baseline atmosphere-ocean dynamics generated by the volcanic eruption. Then we derive favourable conditions for deep-ocean Proudman resonance, and thus extreme meteotsunami surges, at the global scale. Finally, we investigate the aptitude of catastrophic events to generate extreme meteotsunami surges similar to those obtained under Proudman resonance.

Atmosphere-ocean dynamics generated by the Hunga eruption

We carried out a 5-day long simulation of the Lamb wave-driven ocean waves generated by the Hunga eruption (Baseline simulation, hereafter) by coupling off-line the atmospheric model TIGAR (*24*) (Transient Inertia-Gravity And Rossby wave dynamics model) with the global ocean model ATAL (Atmospheric Tsunamis Associated with Lamb waves).

The simulated atmosphere-ocean dynamics is qualitatively described with the animation of the first 48 hours of the Baseline simulation (Movie S1 in supplementary material). TIGAR reproduces the atmospheric Lamb waves with amplitudes reaching up to 7 hPa near the source and 0.5-3 hPa worldwide, in good agreement with the microbarograph observations. The modelled Lamb wave speed is about 318 m/s (*23*), similar to that estimated for the Krakatoa eruption in 1883 (*25*). Used with realistic topography, TIGAR also emulates some wave deformations observed by satellites (*7, 23*) as the Lamb wave travels around the world multiple times. In the ocean, away from the shore, the meteotsunamis simulated by ATAL travel at a speed similar to the Lamb wave and have amplitudes of 1-3 cm in the deep-ocean and up to 5 cm near the source. As less than 1 % of the ocean depths are greater than 6000 m, the Froude number is almost always greater than 1.3 and not favourable to Proudman resonance for Lamb wave-driven meteotsunamis. Consequently, away from the shore, the planetary meteotsunami waves are not amplified by resonance and their amplitudes depend only on the intensity of the atmospheric forcing. However, nearshore wave transformations such as shoaling, reflection, refraction, and diffraction (*26*) are the main drivers of the meteotsunami surges along the coastlines. Additionally, ATAL produces secondary deep-ocean waves with amplitudes larger than the primary meteotsunamis. This sequencing process is well-documented in the tsunami-research community and is caused by the irregular bathymetry of the ocean basins which leads to multipathing as well as focusing/defocusing of the planetary meteotsunami waves (*27*).

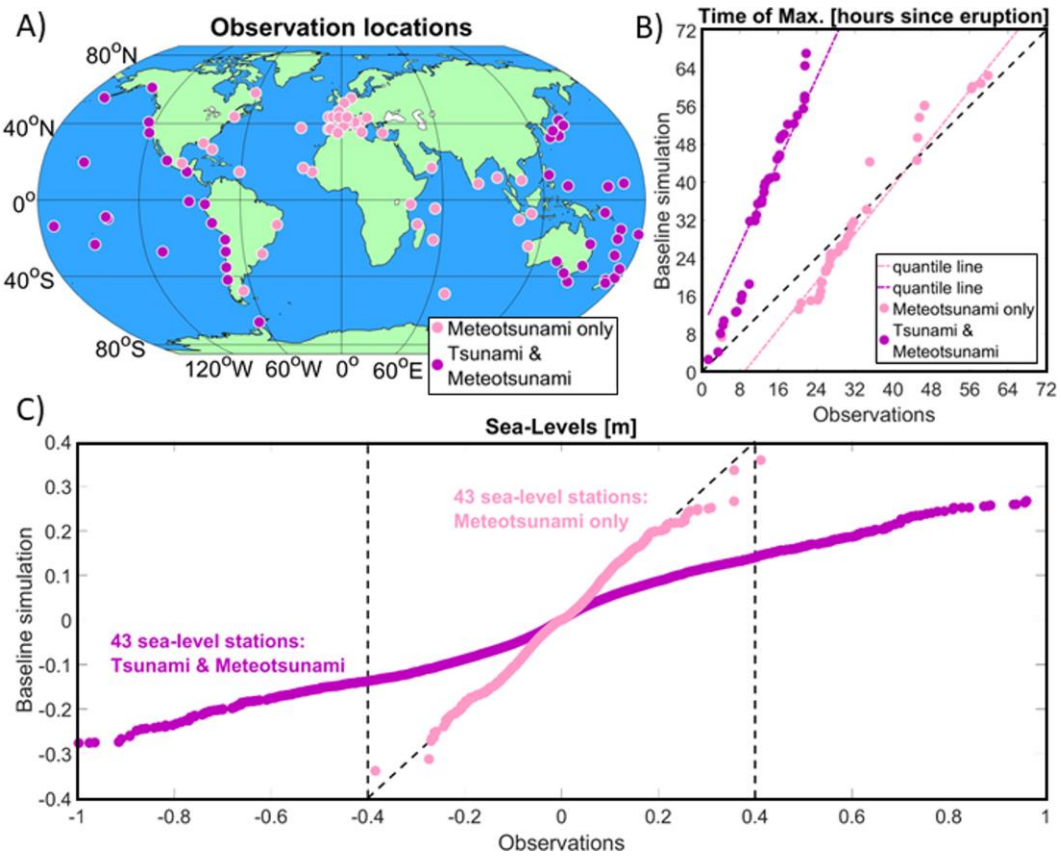

Fig. 1. Validation of the numerical simulation of Lamb wave-driven meteotsunamis generated during 5 days after the Hunga eruption. (**A**) Worldwide stations, and quantile-quantile plots of observed and simulated (**B**) time of the meteotsunami surges (Time of Max.) and

(**C**) 3-min sea levels at 43 stations affected by meteotsunamis only and 43 stations affected by both tsunamis and meteotsunamis.

Quantitatively, ATAL reproduces very well the distribution of the 3-min coastal sea level observations (Meteotsunamis only, Fig. 1, A and C) recorded at 43 tide-gauge locations not affected by tsunamis due to the volcanic eruption (volcanic tsunamis hereafter). For the 43 other tide-gauge stations located mostly in the Pacific Ocean (Tsunami and Meteotsunami, Fig. 1, A and C), the simulated meteotsunamis are about 2-3 times smaller than the observed volcanic tsunamis. A relatively small mismatch in timing exists between the meteotsunami surges in the Baseline simulation and the observations (Fig. 1B). This is mostly explained by the fact that the nearshore wave transformation is not properly represented by the 1.5 km coastal resolution of the ATAL model. For the Tsunami and Meteotsunami stations, the observed maximum sea levels agree with the arrival of the volcanic tsunamis in the first 24 hours after the eruption, while the simulated meteotsunami surges occur during the first 72 hours of simulation. The maximum sea levels during the first 48 hours of the Baseline simulation are presented in Figure 2. Meteotsunamis are higher than 5 cm only near the source of the eruption in the deep-ocean, along the coastlines directly hit by the waves (e.g., Japan, east North America) or close to the focal point of the atmospheric Lamb waves in the northwest Africa (Fig. 2A). Deep-ocean amplifications up to 3 cm occur along changing bathymetry, such as the Southern Pacific ridges, capable to transfer and channel the wave energy over long distances (*28*). The cumulative density function (CDF; Fig. 2B) shows that meteotsunami surges above 20 cm hit less than 1 % of the worldwide coastal areas. Consequently, we find that meteotsunami surges generated by the Hunga eruption could not pose any significant threat to the coastal communities, although strong coastal currents (i.e., rip currents) associated with meteotsunamis of moderate amplitude can be responsible for drowning (*29*).

Tenfold meteotsunami amplification under resonance

To identify the necessary atmospheric conditions for deep-ocean Proudman resonance and, hence, the maximal amplification of the planetary meteotsunami waves, we divided the Lamb wave speed, simulated by TIGAR in the Baseline simulation, by a scaling factor r ranging from $r = 1.25$ ($U \approx 254$ m/s) to $r = 5.00$ ($U \approx 64$ m/s). We then forced a total of 10 additional ATAL simulations of 48-hour length with the obtained atmospheric waves.

Resulting CDF distributions of the meteotsunami surges (Fig. 2B) show that the most extreme meteotsunami surges occur for scaling factors between $r = 1.50$ and $r = 1.65$, and thus for atmospheric waves with phase speeds between $U \approx 193$ m/s and $U \approx 212$ m/s. Under these conditions, 30 % of the worldwide coastlines are hit by meteotsunami surges higher than 35 cm (the 99.9^{th} percentile value of the Baseline simulation). More importantly, the highest meteotsunami surges are obtained for $r = 1.50$ ($U \approx 212$ m/s), which is consequently assumed to be the condition most favourable to Proudman resonance. Additionally, as the ocean depths strongly impact the resonance, the meteotsunami amplification is highly geographically dependent, even under full Proudman resonance ($r = 1.50$; Fig. 2C). It is particularly pronounced west of the northwest American coast where the maximum sea levels are 15 times greater than in the Baseline simulation. Somewhat weaker, but still a significant meteotsunami amplification (i.e., about 80 to 90 %), is obtained in the shallower oceans and seas (e.g., the Arctic Ocean and the Mediterranean Sea).

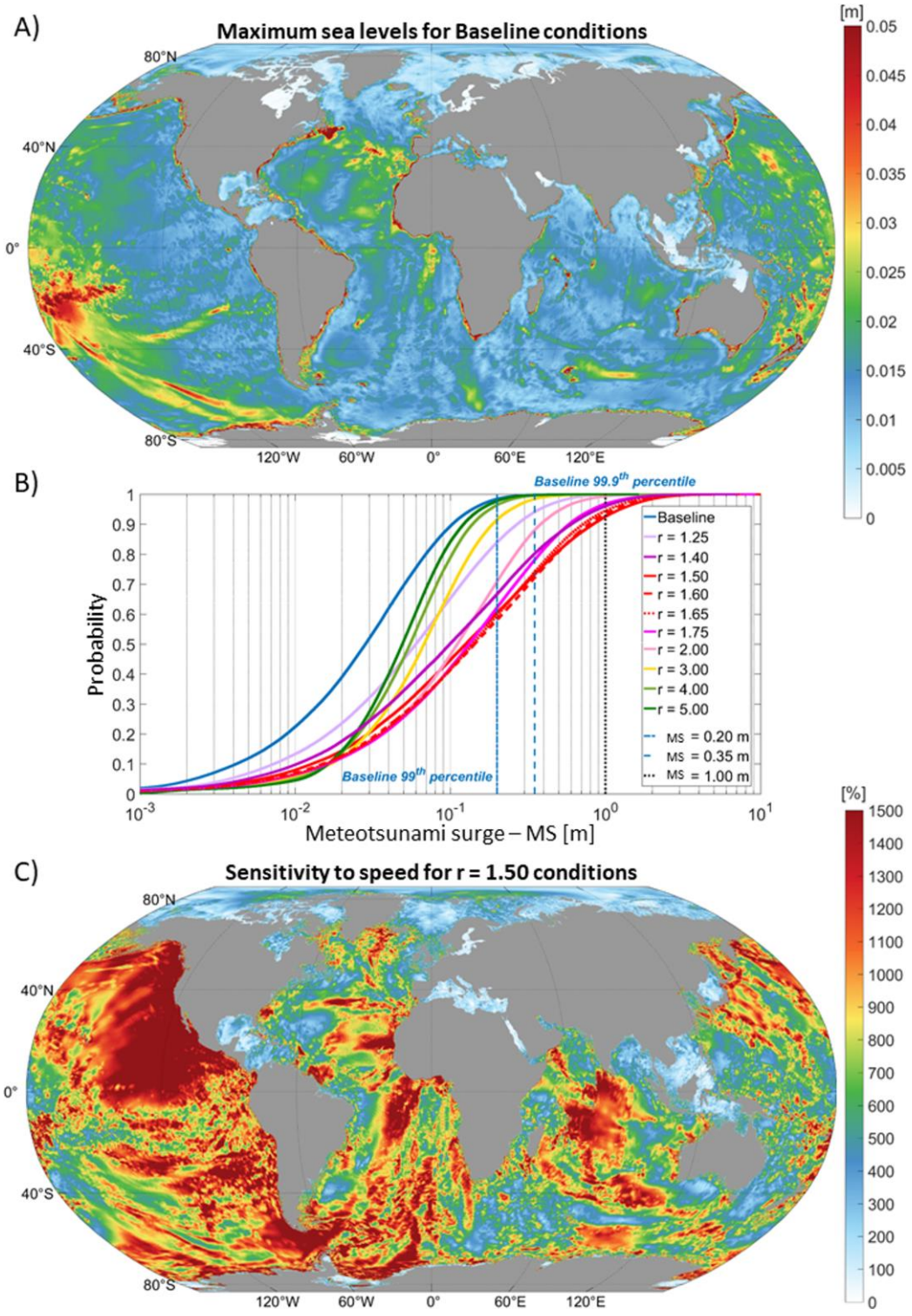

Fig. 2. Distributions of the maximum sea levels after 48 hours of simulation. (**A**) Baseline simulation (r = 1.00), (**B**) cumulative density functions of the meteotsunami surges (MS) for Baseline and sensitivity simulations with scaling factor r applied to the atmospheric wave phase speed varying between 1.25 and 5.00, and (**C**) sea level ratios between the r = 1.50 conditions and the Baseline simulation multiplied by 100 %. Scaling factor r = 1.50 generates the highest meteotsunami surges.

For atmospheric phase speeds obtained with $r \leq 1.40$ or $r \geq 1.75$ (i.e., conditions out of Proudman resonance), the occurrences of meteotsunami surges above 1.00 m are small (below 4.5 %) and even close to zero for $r = 1.25$ and $r \geq 3.00$ (Fig. 3B). Additionally, for $r \geq 3.00$, the spatial coverage of the resonance favourable conditions is reduced to coastal and shelf regions too narrow to allow for strong coastal amplifications.

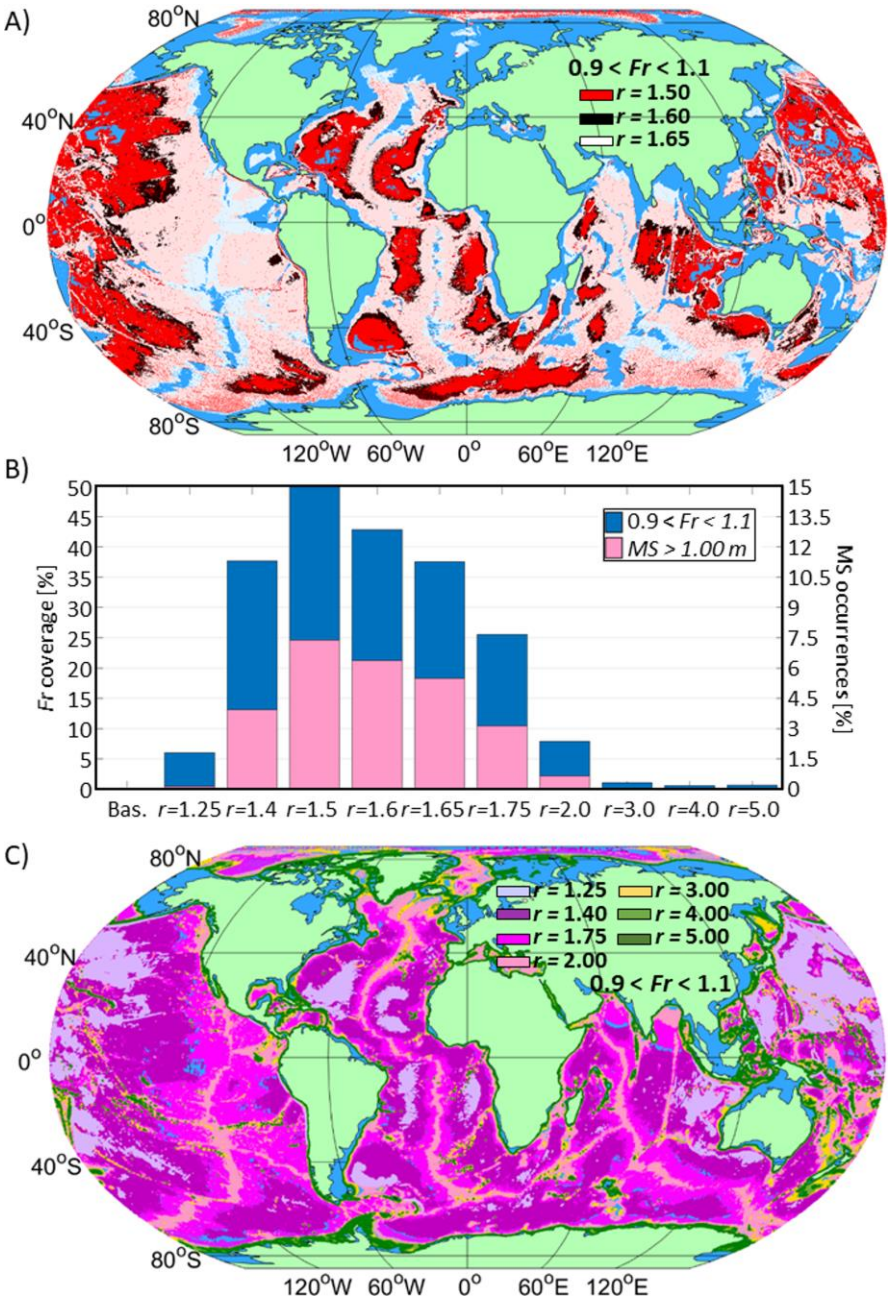

Fig. 3. Distributions of the Froude numbers favorable to Proudman resonance (0.9 < *Fr* < 1.1). Spatial plots for the (**A**) highest (r = 1.50, 1.60, 1.65) and (**C**) lowest (r = 1.25, 1.75, 2.00, 3.00, 4.00, 5.00) resonance conditions and (**B**) spatial coverage (i.e., area favorable to Proudman resonance vs. total area) compared to the occurrences of meteotsunami surges (MS) above 1.00 m.

Finally, for the resonance favourable conditions ($r=1.50$ to $r=1.65$), 35 to 50 % of the whole oceans have Froude numbers close to 1.0 ($0.9<Fr<1.1$) while 5.5 to 7.5 % of the worldwide coastlines are hit by meteotsunami surges larger than 1.00 m (Fig. 3, A and B) and up to 10 m at some locations (Fig. 2B). Further, a strong spatial correlation also exists between the maximal meteotsunami amplifications (Fig. 2C) and the resonance favourable conditions for $r=1.50$ to $r=1.65$ (Fig. 3A). In terms of coastal hazards, we thus find that, under full Proudman resonance, meteotsunami surges can reach similar heights (i.e., more than 1 m and up to 10 m) but are likely to hit more coastal areas (i.e., more than 7 % of the worldwide coastlines) than during catastrophic tsunami events.

Implications in terms of meteotsunami hazards

The condition for full Proudman resonance cannot be reached by the Lamb waves always travelling at $U\approx 318$ m/s. However, based on records of catastrophic events in the Earth's history (*2, 3*), we argue that volcanic eruptions, asteroid impacts and explosions of anthropogenic origin have the potential to generate intense planetary meteotsunami waves. On the one hand, in the case of the Hunga volcano, seismoacoustic and satellite observations (*7, 23*) suggest the presence of several internal gravity waves generated during the first hours after the explosion and likely due to a complex eruption sequence (*23*). They were travelling with speeds between 240 and 270 m/s lower than the Lamb wave but still not favourable to Proudman resonance (i.e., corresponding to $r=1.25$). Nonetheless, the speed of these internal waves is thought to be largely controlled by the vertical profile of the temperature perturbation introduced by the eruption. This suggests that under favourable conditions (e.g., a steeper initial temperature anomaly profile above the tropopause), large amplitude waves with speeds favourable to Proudman resonance can be generated. On the other hand, supervolcanos or asteroid impacts (*2, 5*) – estimated to have return periods of 100-1000 years (*30*) – have the potential to generate fast atmospheric waves as they release about 10 to 1 billion megatons of energy (i.e., 700 to 70 billion times the energy of the atomic bomb dropped on Hiroshima, Japan, in 1945). For example, the Krakatoa eruption of 1883 released 20-50 times more energy than the Hunga eruption (*31*) and generated stronger meteotsunamis in the Atlantic Ocean (*32*). It is therefore possible that more intense atmospheric forcing could lead to meteotsunami surges similar to those obtained under Proudman resonance.

To quantify this effect, an additional ATAL simulation was forced by Lamb waves (travelling at the speed $U\approx 318$ m/s) with 10 times greater amplitude (simulation A) than in the simulation under Proudman resonance (i.e., $r=1.50$; simulation P). Qualitatively, the deep-ocean meteotsunami amplification is similar (up to 20 cm) for both simulations (A and P), but the propagation and coastal amplification processes are visibly different (Movie S2 in supplementary material). Simulation P develops meteotsunamis following the passage of the Lamb waves in the deep-ocean. These waves are strongly modified in the nearshore and coastal areas, where their reflection leads to large amplitude increase over nearly the entire ocean basins (e.g., along the west coast of North America). In contrast, in simulation A (similarly to the Baseline simulation), the main Lamb-wave driven meteotsunamis are followed by secondary waves of higher amplitudes in all ocean basins and no strong reflection occurs near the coasts where the waves are amplified mostly through shoaling, refraction and diffraction.

Quantitatively, in the deep-ocean, the differences in maximum sea levels (A-P; Fig. 4A) exceed 10 cm in the vicinity of the eruption as well as in the Oceania, the Mediterranean Sea, and the north Atlantic basin. However, at the locations where strong reflection occurs in simulation P, they are below -10 cm (e.g., along the northwest-southwest American coasts). Nonetheless, the CDF distributions and the percentage of coastlines with meteotsunami surges higher than 1.00 m

are almost identical for both simulations (Fig. 4B). This shows that, along the coasts, the meteotsunami amplification driven by tenfold amplified Lamb waves matches the conditions under full Proudman resonance.

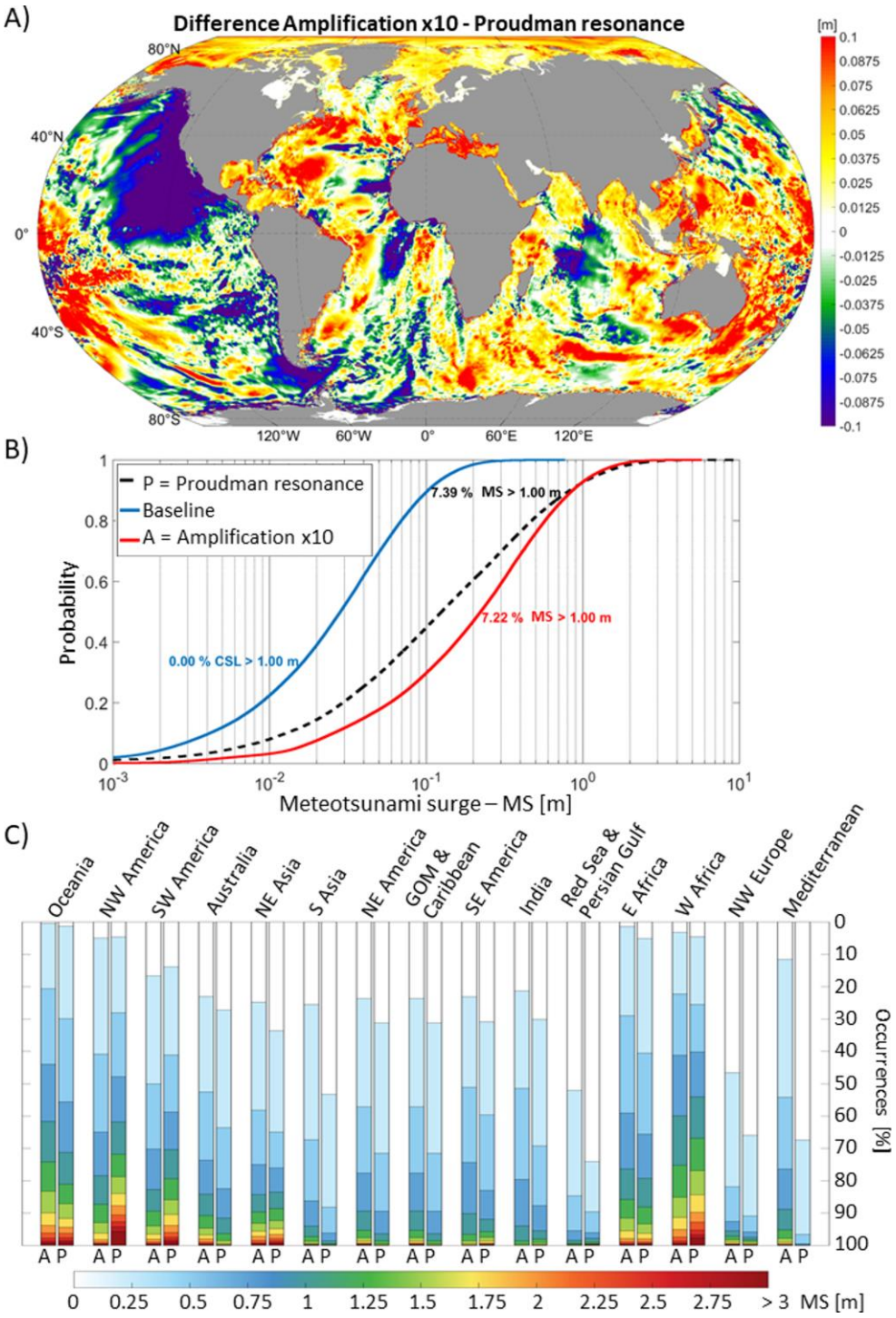

Fig. 4. Maximum sea levels obtained under Proudman resonance conditions (i.e., r = 1.50) and tenfold amplification of the Lamb wave amplitudes in the atmosphere. (**A**) Spatial plot of differences and meteotsunami surges as (**B**) cumulative density functions and (**C**) distributions by coastal sub-domains.

Additionally, the distributions of meteotsunami surges along different coastal regions (Fig. 4C) confirm that the strong reflection of the meteotsunamis in simulation P also impacts the coastal hazards. Indeed, the occurrences of extreme values above 1.50 m are 2-5 times higher in simulation P than in simulation A for the northwest and southwest Americas and west African coastal areas. In contrast, simulation A generates 5 to 8 % of extreme values above 1.50 m in microtidal semi-enclosed basins (e.g., Mediterranean Sea, Gulf of Mexico) not affected by simulation P. As these low-lying coastal areas are well-populated, the modelled meteotsunami surges could pose a serious danger to the coastal communities.

In summary, the destructive potential of the planetary meteotsunami waves remained mostly unexplored before the Hunga eruption. In this study we have demonstrated, for the very first time, that atmospheric planetary waves with phase speeds matching the deep-ocean Proudman resonance criterion or having a large amplitude, can produce extreme surges worldwide. Further, contrarily to the near-field tsunamis, meteotsunami surges can cause serious damage to the coastal infrastructure, sink boats in harbours and take a heavy toll in human lives, at numerous locations along the shores far away from the epicentre of a catastrophic event. Such scenario is even possible for inland events such as the Tunguska explosion (*33*). Consequently, the till now underestimated meteotsunami hazards should be properly assessed and quantified to better prepare for the next big events generating planetary-scale fast atmospheric waves.

References and Notes

1. B.H. Choi *et al.*, Simulation of the trans-oceanic tsunami propagation due to the 1883 Krakatau volcanic eruption. *Nat. Hazards Earth Syst. Sci.* **3**, 321-332 (2003). https://doi.org/10.5194/nhess-3-321-2003
2. C.R. Chapman, D. Morrison, Impacts on the Earth by asteroids and comets: assessing the hazard. *Nature* **367**, 33-40 (1994). https://doi.org/10.1038/367033a0
3. J.V. Morgan *et al.*, The Chicxulub impact and its environmental consequences. *Nat. Rev. Earth Environ.* (2022). https://doi.org/10.1038/s43017-022-00283-y
4. C. Kharif, E. Pelinovsky, Asteroid impact tsunamis. *C. R. Phys.* **6**, 361-366 (2005). https://doi.org/10.1016/j.crhy.2004.12.016
5. S. Ohno *et al.*, Production of sulphate-rich vapour during the Chicxulub impact and implications for ocean acidification. *Nature Geosci.* **7**, 279–282 (2014). https://doi.org/10.1038/ngeo2095
6. D.A. Kring, H.J. Melosh, D.M. Hunten, Impact-induced perturbations of atmospheric sulfur. *Earth Planet. Sci. Lett.* **140**, 201-212 (1996). https://doi.org/10.1016/0012-821X(96)00050-7
7. R. S. Matoza *et al.*, Atmospheric waves and global seismoacoustic observations of the January 2022 Hunga eruption, Tonga. *Science* (2022). https://doi.org/10.1126/science.abo7063
8. K.C. Yeh, C. H. Liu, Acoustic-gravity waves in the upper atmosphere. *Rev. Geophys.* 12, 193-216 (1974). https://doi.org/10.1029/RG012i002p00193
9. H. Lamb, On atmospheric oscillations. *Proc. R. Soc. London Ser. A* 84, 551–572 (1911). https://doi.org/10.1098/rspa.1911.0008
10. F. Bretherton, Lamb waves in a nearly isothermal atmosphere. *Q. J. Roy. Meteorol. Soc.* **95**, 754-757 (1969). https://doi.org/10.1002/qj.49709540608
11. M. Dragoni, D. Santoro, A model for the atmospheric shock wave produced by a strong volcanic explosion. *Geophys. J. Int.* **222**, 735-742 (2020). https://doi.org/10.1093/gji/ggaa205

12. F. Press, D. Harkrider, Air-sea waves from the explosion of Krakatoa. *Science* **154**, 1325-1327 (1966). https://doi.org/10.1126/science.154.3754.1325
13. A. Amores *et al.*, Numerical simulation of atmospheric Lamb waves generated by the 2022 Hunga-Tonga volcanic eruption. *Geophys. Res. Lett.* **49**, e2022GL098240 (2022). https://doi.org/10.1029/2022GL098240
14. G. Harrison, Pressure anomalies from the January 2022 Hunga Tonga–Hunga Ha'apai eruption. *Weather* **77**, 87-90 (2022). https://doi.org/10.1002/wea.4170
15. J.M. Forbes *et al.*, Lamb waves in the lower thermosphere: Observational evidence and global consequences. *J. Geophys. Res. Space Phys.* **104**, 17107-17115 (1999). https://doi.org/10.1029/1999JA900044
16. C.B. Pattiaratchi, E.M.S. Wijeratne, Are meteotsunamis an underrated hazard?. *Philos. Trans. R. Soc. A* **373**, 20140377 (2015). https://doi.org/10.1098/rsta.2014.0377
17. A.B. Rabinovich, Twenty-seven years of progress in the science of meteorological tsunamis following the 1992 Daytona Beach event. *Pure Appl. Geophys.* **177**, 1193–1230 (2020). https://doi.org/10.1007/s00024-019-02349-3
18. K. Satake *et al.*, History and features of trans-oceanic tsunamis and implications for paleo-tsunami studies. *Earth-Sci. Rev.* **202**, 103112 (2020). https://doi.org/10.1016/j.earscirev.2020.103112
19. D. Adam, Tonga volcano eruption created puzzling ripples in Earth's atmosphere. *Nature* **601**, 497 (2022). https://doi.org/10.1038/d41586-022-00127-1
20. S. Self, M.R. Rampino, The 1883 eruption of Krakatau. *Nature* **294**, 699-704 (1981). https://doi.org/10.1038/294699a0
21. I. Vilibić, Numerical simulations of the Proudman resonance. *Cont. Shelf Res.* **28**, 574–581 (2008). https://doi.org/10.1016/j.csr.2007.11.005
22. J. Proudman, The effects on the sea of changes in atmospheric pressure. *Geophys. Suppl. Mon. Not. Roy. Astronom. Soc.* **2**(4), 197–209 (1929). https://doi.org/10.1111/j.1365-246X.1929.tb054 08.x
23. C. Wright *et al.*, Tonga eruption triggered waves propagating globally from surface to edge of space. [Preprint] *Earth and Space Science Open Archive* (2022). https://doi.org/10.1002/essoar.10510674.1
24. S. Vasylkevych, N. Žagar, A high-accuracy global prognostic model for the simulation of Rossby and gravity wave dynamics. *Q. J. Roy. Meteorol. Soc.* **147**, 1989-2007 (2021). https://doi.org/10.1002/qj.4006
25. G.I. Taylor, Waves and tides in the atmosphere. *Proc. R. Soc. Lond. A* **126**, 169–183, 290 (1929).
26. V. Titov *et al.*, The global reach of the 26 December 2004 Sumatra tsunami. *Science* **309**, 2045-2048 (2005). https://doi.org/10.1126/science.1114576
27. E.A. Okal. C.E. Synolakis, Sequencing of tsunami waves: why the first wave is not always the largest, *Geophys. J. Int.* **204**(2), 719–735 (2016). https://doi.org/10.1093/gji/ggv457
28. E.A. Okal, C.E. Synolakis, Far-field tsunami hazard from mega-thrust earthquakes in the Indian Ocean. *Geophys. J. Int.* **172**, 995-1015 (2008). https://doi.org/10.1111/j.1365-246X.2007.03674.x
29. A. Linares *et al.*, Unexpected rip currents induced by a meteotsunami. *Sci. Rep.* **9**, 2105 (2019). https://doi.org/10.1038/s41598-019-38716-2

30. B.G. Mason, D.M. Pyle, C. Oppenheimer, The size and frequency of the largest explosive eruptions on Earth. *Bull. Volcanol.* **66**, 735-748 (2004). https://doi.org/10.1007/s00445-004-0355-9
31. D.J. Lowe, W.P. de Lange, Volcano-meteorological tsunamis, the c. AD 200 Taupo eruption (New Zealand) and the possibility of a global tsunami. *Holocene* **10**, 401-407 (2000). https://doi.org/10.1191/095968300670392643
32. E. Pelinovsky *et al.*, Analysis of tide-gauge records of the 1883 Krakatau tsunami. In: Satake, K. (ed) Tsunamis. Advances in Natural and Technological Hazards Research, vol. 23, 57-77, Springer, Dordrecht (2005). https://doi.org/10.1007/1-4020-3331-1_4
33. C. Chyba, P. Thomas, K. Zahnle, The 1908 Tunguska explosion: atmospheric disruption of a stony asteroid. *Nature* **361**, 40–44 (1993). https://doi.org/10.1038/361040a0
34. F. Press, D. Harkrider, Propagation of acoustic-gravity waves in the atmosphere. *J. Geophys. Research* **67** (10), 3889-3908 (1962). https://doi.org/10.1029/JZ067i010p03889
35. A. Kasahara, Numerical integration of the global barotropic primitive equations with Hough harmonic expansions. *J. Atmos. Sci.* **34**, 687-701 (1977).
36. S.E. Cohn, D.E. Dee, An analysis of the vertical structure equation for arbitrary thermal profiles. *Q. J. Roy. Meteorol. Soc.* **115**, 143–171 (1989). https://doi.org/10.1002/qj.49711548508
37. C.C. Stephan, N. Žagar, T.G. Shepherd, Waves and coherent flows in the tropical atmosphere: New opportunities, old challenges. *Q. J. Roy. Meteorol. Soc.* **147**, 2597-2624 (2021). https://doi.org/10.1002/qj.4109
38. S.M. Cox, P.C. Matthews, Exponential time differencing for stiff systems. *J. Comp. Physics* **176**(2), 430-455 (2002). https://doi.org/10.1006/jcph.2002.6995
39. D. Themens *et al.*, Global propagation of ionospheric disturbances associated with the 2022 Tonga volcanic eruption. *Geophys. Res. Lett.* **49**, e2022GL09815 (2022). https://doi.org/10.1029/2022GL098158
40. R.A. Luettich, R.H. Birkhahn, J.J. Westerink, Application of ADCIRC-2DDI to Masonboro Inlet. A brief numerical modeling study. Contractors Report to the US Army Engineer Waterways Experiment Station: North Carolina (1991).
41. W.J. Pringle, D. Wirasaet, K.J. Roberts, J.J. Westerink, Global storm tide modeling with ADCIRC v55: unstructured mesh design and performance. *Geosci. Model Dev.* **14**, 1125–1145 (2021). https://doi.org/10.5194/gmd-14-1125-2021
42. C. Denamiel *et al.*, The Adriatic Sea and coast modelling suite: evaluation of the meteotsunami forecast component. *Ocean Model.* **135**, 71-93 (2019). https://doi.org/10.1016/j.ocemod.2019.02.003
43. C. Denamiel *et al.*, Uncertainty propagation using polynomial chaos expansions for extreme sea level hazard assessment: the case of the eastern Adriatic meteotsunamis. *J. Phys. Oceanogr.* **50**(4), 1005-1021 (2020). https://doi.org/10.1175/JPO-D-19-0147.1
44. C. Denamiel, I. Tojčić, I. Vilibić, Meteotsunamis in orography-free, flat bathymetry and warming climate conditions. *J. Geophys. Res: Oceans* **127**, e2021JC017386 (2022). https://doi.org/10.1029/2021JC017386
45. K.J. Roberts, W.J. Pringle, J.J. Westerink, OceanMesh2D 1.0: MATLAB-based software for two-dimensional unstructured mesh generation in coastal ocean modelling. *Geosci. Model Dev.* **12**, 1847–1868 (2019). https://doi.org/10.5194/gmd-12-1847-2019

46. P. Wessel, W.H.F. Smith, A global, self-consistent, hierarchical, high-resolution shoreline database. *J. Geophys. Res.* **101**(B4), 8741–8743 (1996). https://doi.org/10.1029/96JB00104
47. GEBCO Compilation Group. GEBCO 2021 Grid [dataset] (2021). https://doi.org/10.5285/c6612cbe-50b3-0cff-e053-6c86abc09f8f
48. P.G. Holland, Manning formula. In: Encyclopedia of Hydrology and Lakes. Encyclopedia of Earth Science. Springer, Dordrecht (1998). https://doi.org/10.1007/1-4020-4497-6_149
49. Flanders Marine Institute (VLIZ). Intergovernmental Oceanographic Commission (IOC) (2022): Sea level station monitoring facility. [Dataset] *VLIZ* (2022). https://doi.org/10.14284/482
50. C. Denamiel, Destructive potential of planetary meteotsunami waves: ATAL ocean model results. [Dataset] *Zenodo* (2022).
51. W.J. Pringle, Global Storm Tide Modeling on Unstructured Meshes with ADCIRC v55 - Simulation Results and Model Setup. [Dataset] *Zenodo* (2020). https://doi.org/10.5281/zenodo.3911282
52. W.J. Pringle, K. Roberts, CHLNDDEV/OceanMesh2D: OceanMesh2D V3.0.0. [Dataset] *Zenodo* (2020). https://doi.org/10.5281/zenodo.3721137

Acknowledgments:

CD and IV acknowledges the support of the European Centre for Medium-range Weather Forecasts (ECMWF) which provided staff assistance, with a special thanks to Xavier Abellan and Carsten Maass, as well as the computing and archive facilities used in this research through the Special Project “Using stochastic surrogate methods for advancing towards reliable meteotsunami early warning systems”. NŽ and SV thank Ingo Lange for providing the Barbados pressure records, Bernhard Mayer for compiling the pressure data from https://luftdaten.info/ (last accessed on 1 June 2022) and to Andreas Rhodin for help with data processing.

Funding:

The TIGAR model development was supported by the Ideen und Risiko Fund of Universität Hamburg.

Author contributions:

Conceptualization: IV, CD

Methodology: CD, IV

Investigation: CD, IV, SV, NŽ, PZ

Visualization: CD

Project administration: CD, IV

Writing – original draft: CD, IV

Writing – review & editing: CD, IV, SV, NŽ, PZ

Competing interests:

The authors declare that they have no competing interests.

Data and materials availability:

Sea level data is provided by the UNESCO Intergovernmental Oceanographic Commission (IOC) Sea Level Station Monitoring Facility (*49*) at https://www.ioc-sealevelmonitoring.org/ (last accessed on 1 June 2022). Ocean model results are archived on Zenodo (*50*) at https://doi.org/10.5281/zenodo.6503338. The ADCIRC v55 code updated for global applications is archived on Zenodo (*51*) at https://doi.org/10.5281/zenodo.3911282. The OceanMesh2D V3.0.0 code used to generate the ATAL mesh is archived on Zenodo (*52*) at https://doi.org/10.5281/zenodo.3721137.

Supplementary Materials

Materials and Methods

References (35–49)

Movies S1 to S2

Science
AAAS

Supplementary Materials for

Destructive potential of planetary meteotsunami waves beyond the Hunga volcano eruption (Tonga)

Cléa Denamiel, Sergiy Vasylkevych, Nedjeljka Žagar, Petra Zemunik, Ivica Vilibić

Correspondence to: cdenami@irb.hr

This PDF file includes:

Materials and Methods
Captions for Movies S1 to S2

Other Supplementary Materials for this manuscript include the following:

Movies S1 to S2

Materials and Methods

Numerical experiments

A total of 12 different simulations are analysed in this study. First, the Baseline simulation is reproducing as realistically as possible the Lamb waves in the atmosphere and the meteotsunamis in the ocean for a 5-day long period after the Hunga eruption. Then, ten 2-day long process-oriented simulations are performed in order to find the speeds of the atmospheric waves leading to the maximum meteotsunami amplification under full Proudman resonance. For these simulations, the timeline of the Baseline atmospheric response is artificially rescaled by 1.25, 1.40, 1.50, 1.60, 1.65, 1.75, 2.00, 3.00, 4.00 and 5.00, thereby proportionally reducing the speed of the Lamb waves. The simulation leading to full Proudman resonance is referred to as simulation P. Finally, in the last 2-day long simulation (simulation A) used to assess the destructive potential of truly catastrophic events, the amplitude of the Lamb waves used in the Baseline simulation is multiplied by 10 before forcing the ocean model.

Atmospheric response in Transient Inertia–Gravity And Rossby wave dynamics (TIGAR) model

A Lamb wave is an acoustic-gravity wave mode often considered in the isothermal atmosphere at rest. The non-dispersive Lamb waves propagate horizontally with a phase velocity weakly depending on the vertical background temperature profile. For a standard atmosphere, this speed is $U \approx 312$ m/s (*14*, *34*). In the barotropic framework (*35*), a horizontally propagating surface gravity wave has a phase speed $c = \sqrt{gD}$, where D is the mean fluid depth. This approach extends into the baroclinic atmosphere, where D becomes the equivalent depth, or the eigenvalue of the vertical structure equation for the linearized primitive equations (*36*), associated with a single vertical mode, an eigenvector of the vertical structure equation. Cohn and Dee (*36*) showed that the global, bounded atmosphere has the equivalent depth $D \approx 10$ km, with associated gravity wave speed $c \approx 313$ m/s. This matches the speed of the main wave triggered by volcanic eruptions.

The above observation supports the use of the barotropic version of the TIGAR model (*24*, *37*) for the Lamb wave simulation after the Hunga eruption. The TIGAR model solves the primitive equations in terrain-following coordinates using the Hough harmonics as the basis functions. In this representation, the Rossby and inertia–gravity waves are prognostic quantities, an approach especially suitable for studying gravity wave dynamics on the sphere. The model includes a realistic orography on the computational grid T170 that corresponds to the regular Gaussian grid of 680 and 320 grid points in the longitudinal and latitudinal directions, respectively. Presence of orography ensures the deflection of the Lamb wave by major mountain ranges (video S1 in supplementary material). The exponential 4th order Runge-Kutta scheme (*38*) with a 3-min time step was used for time integration. The dissipative processes were represented through the linear damping term in the continuity equation with damping scale defined by a tuning parameter τ.

The Hunga eruption was modelled by specifying an initial condition in the form of large amplitude Gaussian geopotential height perturbation centred on the volcano location, superimposed on the barotropic atmosphere at rest. Noting that in the barotropic model the geopotential height and pressure perturbations are proportional, the amplitude of the pressure perturbation at the source $\Delta p = 35.1$ hPa and the scale parameter $\sigma = 2.7°$ were optimized to match the observed wavelength of the wave response, while the dissipation time scale $\tau = 3.4$ days was obtained by best fit of the wave amplitude to the observed pressure fluctuations at the evaluation

sites. Finally, the ability of the TIGAR model to reproduce the observed Lamb wave generated during the Hunga event has been thoroughly evaluated in a previous study (*39*).

Atmospheric Tsunamis Associated with Lamb waves (ATAL) ocean model

The ATAL model was specifically developed and implemented to reproduce the planetary meteotsunami waves generated by intense atmospheric forcing. It is based on the barotropic version (2DDI) of the Advanced CIRCulation (ADCIRC) unstructured model (*40*) which solves the shallow-water equations in the ocean. Recently, the ADCIRC model has been updated for global applications (*41*) and extensively used to study and forecast meteotsunami events (*42*–*44*) at the regional and nearshore scales.

The ATAL unstructured mesh used in this study was designed not only to properly capture the atmosphere-ocean interactions at the basin scale, but also to partially reproduce the coastal and nearshore meteotsunami transformation. It was produced with the OceanMesh2D (*45*) software for resolutions ranging from 20 km in the deep-ocean to 1.5 km along the worldwide coastlines using (1) the Global Self-consistent, Hierarchical, High-resolution Geography Database (GSHHG) fine resolution coastline (*46*) and (2) the bathymetry from the GEBCO_2021 15 arc-second grid (*47*). The final mesh is composed of 6 864 084 nodes forming 13 306 437 triangular elements with a bathymetry ranging from a minimum of 1 m at the coast to 9823 m in the deepest part of the ocean.

In terms of numerical setup, the ATAL model uses the optimal configuration of the ADCIRC model for global simulations (*40*) with a time step of 1 second, a spatially varying Manning friction coefficient (*48*), no tidal forcing, no wind forcing and a 3-min (for the Baseline simulation) pressure forcing adding the Lamb wave oscillations from the TIGAR model to the 1013 hPa uniform background pressure. In its actual configuration, the ATAL model runs on 400 CPUs (i.e., sub-domains) and produces 1 day of simulation in 2 hours of computation on the European Centre for Medium-range Weather Forecasts (ECMWF) High-Performance Computing (HPC) facilities.

Observations and ATAL model evaluation

The ATAL model evaluation is performed, for the sea levels only, over a period of 5 days after the Hunga eruption. First, the 1-minute sea level data at 86 worldwide tide-gauge stations is extracted from the Intergovernmental Oceanographic Commission Sea Level Station Monitoring Facility (*49*). At each of the 86 stations, the high-frequency signal (i.e., mostly the tsunami and meteotsunami waves and the local processes such as harbour resonance) is obtained by using a 2-h Kaiser-Bessel filter on the quality-checked observational data. Second, the 3-min sea level outputs of the Baseline simulation are extracted at the closest mesh node from the 86 station locations and the 1-min measurements are resampled to 3-min. The evaluation of the sea level heights is thus performed for 86 observation-model pairs of 2401-point long records including potentially missing data. Third, for the comparison of the times of the maximum, the model and observation maximum sea levels and associated times are extracted for the entire 5-day period at each of the 86 stations. The evaluation is thus only performed for 86 observation-model pairs of "arrival" times. Then, as both tsunami and meteotsunami waves were generated after the eruption and no straightforward method can easily differentiate them in the observations, the tide-gauge stations are separated in two groups: (1) the "Tsunami and Meteotsunami" group, including 43 stations mostly located in the Pacific Ocean, and (2) the "Meteotsunami only" group, including the 43 remaining locations where no tsunami impact was recorded. Finally, as

this process-oriented study focuses more on the general reproduction of the Lamb wave-driven meteotsunami waves at the planetary scale than the precise reproduction of the extreme sea levels and their timing at a precise location, quantile-quantile plots are used for the ATAL model evaluation for the two groups of stations.

Extreme sea level analysis

The outputs of the ATAL model analysed in this study are (1) the 3-min sea levels for Baseline simulation and simulation A as well as the 4.5-min sea levels for simulation P, only used to produce the animations presented in Movies S1 and S2, and (2) the maximum sea levels automatically computed at every time-step and obtained after 2 days of simulation. The maximum sea levels are analysed (1) spatially over the entire ATAL domain and (2) for the ATAL mesh nodes only located along the coastline (referred as meteotsunami surges). The percentages of meteotsunami surge occurrences above 1.00 m are calculated as the ratio between the number of coastal mesh nodes fulfilling the criteria and the total number of coastal mesh nodes multiplied by 100 %. The percentages of Froude coverage are calculated as the ratio between the sum of the areas of each mesh element with 3 mesh nodes fulfilling the criteria and the sum of the areas of all mesh elements multiplied by 100 %.

Movie S1.

Animation of the simulated Lamb wave intensities in the atmosphere and the resulting meteotsunami waves in the ocean during the first 48 hours of the Baseline simulation.

Movie S2.

Animation of the simulated meteotsunami waves obtained under full Proudman resonance (simulation P) and for a tenfold amplification of the Lamb wave intensities (simulation A).